

Detection of the Higgs particle decaying into two photons using Calorimetry at LHC.

Candidacy Paper

John White, *University of Victoria.*

July 18, 1994

Abstract

A simulation of gluon-gluon fusion production and two photon decay of Higgs particles at a proton collider was performed. Detection of the two photon final state by the ATLAS calorimeter system was simulated. The Higgs particle mass, using the invariant mass of the two photon final state, was calculated and the effects of experimental energy and angular resolutions were studied. The Higgs mass reconstruction resolution was found to be $\sim 1\%$ for $90 < m_{H^0} < 200$ GeV with energy resolution as the dominant factor. The effect on the reconstructed Higgs mass by varying the experimental angular and energy resolutions was studied. To maintain a nominal Higgs mass resolution of 1.2% an angular resolution sampling term of $100 \text{ mrad} \cdot \sqrt{E}$ or better is required when using the given experimental energy resolution. Conversely, an energy resolution sampling term of $13\% \cdot \sqrt{E}$ or better is needed to maintain the same nominal mass resolution when using the given experimental angular resolution.

Contents

1	The Standard Model and the Higgs Mechanism	3
1.1	The Standard Model	3
1.2	The Higgs Mechanism	4
2	ATLAS and LHC	5
2.1	LHC	5
2.2	ATLAS	5
3	Higgs signatures at LHC	7
3.1	Higgs production at a proton collider	7
3.2	The $H^0 \rightarrow \gamma \gamma$ decay	8
4	Higgs analysis	9
4.1	Higgs partial widths and branching ratios	9
4.2	Higgs production cross section	9
4.3	Simulation of $H^0 \rightarrow \gamma \gamma$ events	12
4.4	Detector response to $H^0 \rightarrow \gamma \gamma$	16
4.5	Kinematic cuts	17
4.6	Results	17
5	Conclusions	22
A	Partial width formulae	23

1 The Standard Model and the Higgs Mechanism

1.1 The Standard Model

In the manner that the electric and magnetic forces were united by Maxwell in the 1860's, the weak and electromagnetic forces were united by Glashow, Weinberg and Salam in 1961 [1]. The standard model of electroweak interactions between elementary particles is based on a spontaneously broken $SU(2) \times U(1)$ gauge theory [1]. The addition of the $SU(3)$ group that describes strong interactions completes the Standard Model (SM). There are two types of particles in the SM: the fermions that constitute all matter, and the bosons that mediate forces. Gravity is neglected at this energy and distance scale. The forces that govern the behaviour of the fermions are the electromagnetic, the weak and the strong forces. These forces are transmitted by mediators of varying masses: the electromagnetic force by the massless *photon*; the weak force, responsible for β -decays, by massive W^\pm and Z^0 particles [2, 3]; and the strong force, that binds nuclei, by colour charge carrying massless *gluons*.

The fermions are divided into two groups, the leptons and quarks. Leptons and quarks are subdivided again into three generations shown in table 1. Leptons carry integer electric

Table 1: Leptons and quarks arranged in generations of increasing mass. Lepton and quark masses (in this paper $c = \hbar = 1$) from [4]. The evidence for a top quark needs confirmation [5].

Leptons			Quarks		
Name	Mass (MeV)	Charge (e)	Name	Mass (MeV)	Charge (e)
electron (e)	0.511	-1	up	5.6 ± 1.1	+2/3
ν_e	< 0.000017	0	down	9.9 ± 1.1	-1/3
muon (μ)	106	-1	charm	1350 ± 50	+2/3
ν_μ	< 0.27	0	strange	199 ± 33	-1/3
tau (τ)	1784	-1	top	174 ± 16 GeV	+2/3
ν_τ	< 35	0	bottom	~ 5 GeV	-1/3

charge and feel the electroweak force. Quarks carry colour charge and non-integer electric charge and feel the electroweak and strong forces. Due to the structure of the strong force a single free quark can never be observed. Quarks appear in the SM in combinations that give no net colour charge. The fermions have corresponding antifermions. Transitions between quark generations are observed. They are described in the SM with the 3×3 Cabibbo-Kobayashi-Maskawa (CKM) matrix [6].

Following the discovery of the W^\pm and Z^0 vector bosons at the CERN $p\bar{p}$ collider [2, 3], the SM has been tested to unprecedented precision by the experimental results obtained from the four experiments at LEP [7, 8]. The SM proves to be a model capable of precise predictions at the microscopic level. However it is universally accepted that the SM cannot be the last word, although no viable extension of the SM has emerged. Some of the proposed

extensions of the SM, for example Supersymmetry, bring a rich spectrum of particles which await discovery.

1.2 The Higgs Mechanism

In the SM the masses of the bosons and fermions are generated after the spontaneous symmetry breaking of the vacuum via the *Higgs mechanism* [9]. The SM is a gauge theory that is renormalizable, that is divergences caused by higher order effects may be consistently removed.

In general a renormalizable theory cannot have massive particles but the fermions and gauge bosons (W^\pm, Z^0) are massive. This contradiction is solved by realising that the solutions of the SM Lagrangian may violate its inherent symmetry. A complex Higgs scalar doublet (Φ) is added to the SM Lagrangian along with appropriate coupling terms to the fermions. This modified Lagrangian is made locally gauge invariant, ie: it is unchanged when the fields are modified according to their space-time points. The symmetry of the theory is broken by the vacuum of the theory. Gauge invariance [10] of the theory is retained since the Lagrangian is still locally gauge invariant. Breaking the symmetry allows massless particles to acquire mass through coupling to the Higgs field. In the process three of the four degrees of freedom of the Higgs field Φ are absorbed in the W^\pm, Z^0 leaving behind a massive neutral scalar *Higgs boson*.

The Higgs boson (H^0) has not yet been observed experimentally [11], but LEP data [12] has put a lower bound on the Higgs mass of 62.5 GeV. In this situation high energy hadron colliders, such as LHC, which have centre of mass energies in the multi-TeV range, have the best potential for discovery of the Higgs particle.

2 ATLAS and LHC

2.1 LHC

The Large Hadron Collider (LHC) is the next major project planned by CERN [13]. This collider is to be located in the existing LEP tunnel. The colliding particles are protons with a centre-of-mass energy of 14 TeV. A second mode of operation for the LHC as a heavy ion collider will be possible. This collider makes extensive use of the existing facilities at CERN. The constraint of the diameter of the LEP ring places a demand on the guide field of the bending magnets required for LHC operation at 14 TeV, which must be in the region of 8.5 T.

The use of protons as projectiles has the following advantages:

- Synchrotron radiation losses for protons are much less than for electrons of the same energy [13];
- Protons are easier to produce than antiprotons and at high energies the cross section σ_t is equal for pp and $p\bar{p}$ collisions;
- A hadron collider offers excellent discovery potential due to the nature of the collisions. At high energies the proton momentum is split equally between gluons and quarks which allows a diverse spectrum of collisions.

LHC is designed to run at the high particle rate or *luminosity* (defined as the number of particles per cm^2 per second, $\text{cm}^{-2}\text{s}^{-1}$) of $1 \times 10^{34} \text{ cm}^{-2}\text{s}^{-1}$ because the cross sections for the most sought after physics signals are very small.

Characteristically the experiments at LHC consist of large detectors with precise inner tracking, followed by electromagnetic then hadronic calorimetry, and finally muon detectors. The calorimetry must be as hermetic as possible in order to make the detection of missing transverse energy (E_T^{miss}) efficient. These detectors must be physically large to contain the high energy interaction products. They must have a fast response time to cope with the high luminosity and low bunch crossing times of the colliders.

2.2 ATLAS

The ATLAS detector [14, 15] (see figure 1) is designed as a general purpose detector with a balanced approach to detection of electrons, photons, muons, jets and missing transverse energy. The detector is optimized to provide as many signatures as possible for new physics at the highest LHC luminosity, while at the same time retaining good performance at the lower initial luminosities.

At LHC lepton identification is crucial. Even if the final state lepton rate is often expected to be small for many processes, leptons will give the cleanest signals. At a luminosity of $10^{34} \text{ cm}^{-2}\text{s}^{-1}$ there will be very large background rates which can mask these lepton signatures. Muons go through the detector without showering. They can also be separated from jets. Muon momentum is measured by their radius of curvature in a magnetic field. The ATLAS detector at LHC makes use of good calorimetry for electron and photon identification

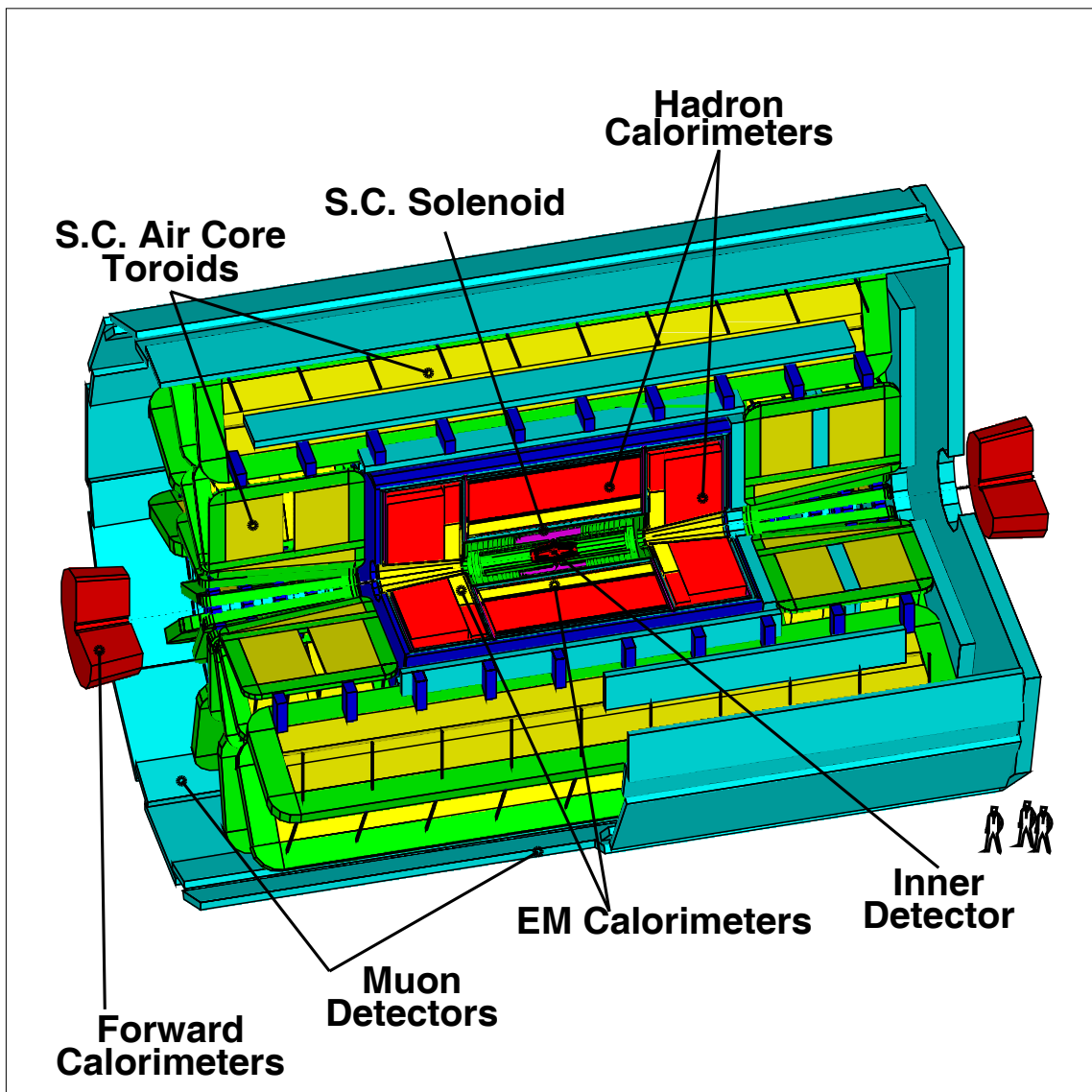


Figure 1: The proposed ATLAS detector.

and E_T^{miss} measurements, which will rely on good measurements of EM shower energy and position over a wide acceptance range. A sophisticated inner tracking system complements the calorimetry in this task and it also provides event vertex information.

3 Higgs signatures at LHC

The mass of the Higgs boson (m_{H^0}) is an important consideration for determining useful detection decay modes [14, 15]. A heavy Higgs boson of $200 \leq m_{H^0} \leq 1000$ GeV has $H^0 \rightarrow W^+ W^-$ or $Z^0 Z^0$ as its dominant decay modes. Detection of these modes requires the ability to detect electrons, muons, neutrinos (through E_T^{miss}) and jets under high luminosity conditions. In the intermediate mass range $120 \leq m_{H^0} \leq 180$ GeV the decay mode $H^0 \rightarrow Z^{0*} Z^0 \rightarrow llll$ is not dominant but is the most promising. The decay $H^0 \rightarrow W^* W$ has a greater width but the $Z^{0*} Z^0$ mode [16] has reducible backgrounds. In the light Higgs range $50 \leq m_{H^0} \leq 200$ GeV the most attractive decay mode is $H^0 \rightarrow \gamma \gamma$. Current data [5] favours this mass range [17]. This mode does not have the largest decay width in this m_{H^0} range but by searching for two highly energetic photons (γ 's) the backgrounds to this decay can be dealt with [20]. Another mode, $H^0 \rightarrow Z^0 \gamma$, could be useful but it suffers from a high irreducible background and a low cross section.

3.1 Higgs production at a proton collider

At a proton collider the Higgs boson will be produced mainly by *gluon-gluon fusion*. The corresponding lowest order diagram is shown in figure 2. Only quarks are in the loop shown

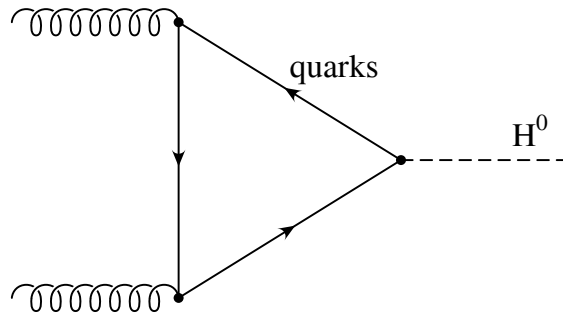


Figure 2: The Feynman diagram of $gg \rightarrow H^0$. The massless gluons couple to the Higgs boson through massive quarks. Only gluons and quarks carry colour charge thus only quarks can appear in the loop.

in figure 2 since only quarks and gluons carry colour charge. The heaviest quarks dominate this process and the cross section is given by equation 1. This cross section is subject to higher order corrections that can increase its value by a factor of ~ 1.7 [18].

At high energies the protons are considered composite particles made up of quarks and gluons, the *partons*. *Structure functions* [19] describe the fraction of the proton longitudinal momentum carried by each group of partons. Structure functions give the probability that a parton carries a momentum fraction 'x'. For gluons the probability is very large at low 'x'.

When two protons collide the gluons in each proton do not usually carry an identical fraction of proton momentum. Thus the Higgs boson is not produced at rest and is boosted longitudinally along the beam line. The Higgs boson can acquire transverse momentum through higher order diagrams where a two body final state is reached [18]. These are

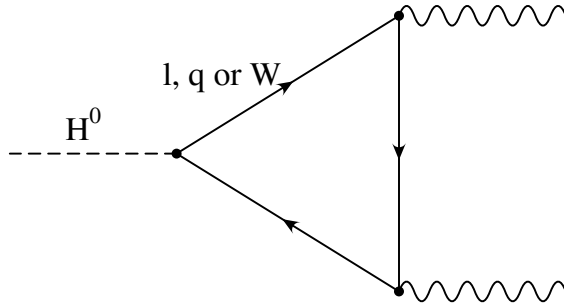


Figure 3: The $H^0 \rightarrow \gamma \gamma$ Feynman diagram. Only electric charge carrying massive particles may appear in the loop that couples the massless photons to the Higgs boson.

known as *real corrections* which occur when gluons are radiated and in gluon-quark and quark-antiquark collisions.

3.2 The $H^0 \rightarrow \gamma \gamma$ decay

The coupling strength of a Higgs boson to a particle is proportional to the particle mass. Thus the $H^0 \rightarrow \gamma \gamma$ decay is mediated by fermion and gauge boson loops as in figure 3. Both the leptons and quarks can be in a fermion loop whereas only the W's contribute to the gauge boson loop since the Z^0 does not carry electric charge. Since the Higgs is a spin 0 particle the γ 's directions are spherically symmetric in the Higgs rest frame.

The backgrounds that can mimic the signature of two energetic photons are [20]:

- Two-photon production from quark annihilation and ‘box’ diagrams. This is the intrinsic background;
- Two-photon production from higher order bremsstrahlung diagrams;
- Electromagnetic energy deposited from a quark or gluon jet rather than a photon.

These backgrounds may be reduced by placing selection criteria or *cuts* on data [20]. A requirement that each photon has a large transverse momentum (P_T) cuts out low energy two-photon background. The photons produced from bremsstrahlung tend to be asymmetric in P_T . A cut requiring approximately equal P_T reduces this background. Since quark or gluon jets tend to carry along many particles, an *isolation cut* requiring low energy in the area surrounding the deposited photon energy reduces this source. In the simulation these backgrounds are not generated but the cuts are used to reflect the difficulty of detecting photons in this environment.

4 Higgs analysis

The production and decay of Higgs boson of m_{H^0} at the LHC pp collider is simulated using a simple Monte Carlo program. The gluon-gluon fusion production mechanism and $H^0 \rightarrow \gamma \gamma$ decay mode is simulated and the Higgs partial widths and gluon-gluon production cross section are calculated. Detection of the resulting photons by ATLAS is simulated.

4.1 Higgs partial widths and branching ratios

The Higgs partial widths (Γ_i) are calculated using the formulae in Appendix A and shown in figure 4 for $50 < m_{H^0} < 200$ GeV using a top quark of 174 GeV. Note that for this mass range the dominant contributions to the total width (Γ) come from the $b\bar{b}$ and W^*W^* partial widths. The effect of running b-quark mass is taken into account [21] and scales the $b\bar{b}$ partial width by a factor of ~ 0.5 compared to using a fixed quark mass. The next most relevant fermion partial width is due to $H^0 \rightarrow c\bar{c}$ and is generally a factor of 10 less than $b\bar{b}$. The c-quark mass is not varied with energy scale [21] here. Above ~ 120 GeV the W^*W^* partial width dominates the total width. Despite the fact that the Higgs boson couplings are proportional to particle mass the W^*W^* partial width dominates the Z^*Z^* . This is due to a $2 \times \cos\theta_w$ term in the denominator of the $H^0 \rightarrow Z^*Z^*$ vertex and cancellations from producing two identical Z^0 bosons. Finite width effects of the W^\pm 's and Z^0 's are taken into account and an increase in both the W^*W^* and Z^*Z^* partial widths is noticed at $m_{H^0} \sim 2m_W$ and $m_{H^0} \sim 2m_Z$ respectively where the real W^\pm and Z^0 channels open up.

The $H^0 \rightarrow \gamma \gamma$ partial width ($\Gamma_{\gamma\gamma}$) contributes very little to the total width. In the Higgs mass range where $H^0 \rightarrow \gamma \gamma$ is interesting Γ is narrow. Thus the Higgs can be considered a narrow resonance and finite width effects can be neglected. Practically this means the production and decay of Higgs bosons in this channel can be considered separate processes in the simulation.

The branching fraction of each decay mode, shown in figure 5, is calculated using

$$BR_i = \frac{\Gamma_i}{\Gamma}$$

where BR_i is the branching fraction of decay mode ‘‘i’’. In figure 5 it can be seen that for $m_{H^0} < \sim 120$ GeV the Higgs boson will decay into b-quark pairs and into W bosons at $m_{H^0} > \sim 120$ GeV. At $m_{H^0} \sim 2m_W$ the W^* 's become real at this pole and other branching fractions decrease, especially $BR_{Z^*Z^*}$. Similarly at $m_{H^0} \sim 2m_Z$ $BR_{Z^*Z^*}$ increases at the expense of other modes. The $H^0 \rightarrow \gamma \gamma$ branching fraction reaches a maximum of 0.2% at $m_{H^0} \sim 120$ GeV.

4.2 Higgs production cross section

The Born level cross section [22] at a pp collider for Higgs boson production through gluon-gluon fusion is calculated using [23]

$$\sigma(pp \rightarrow H^0) = \Gamma_{gg} \frac{\pi^2}{8 m_{H^0}} \tau \int_\tau^1 \frac{dx}{x} f(x, m_{H^0}^2) f\left(\frac{\tau}{x}, m_{H^0}^2\right) \quad (1)$$

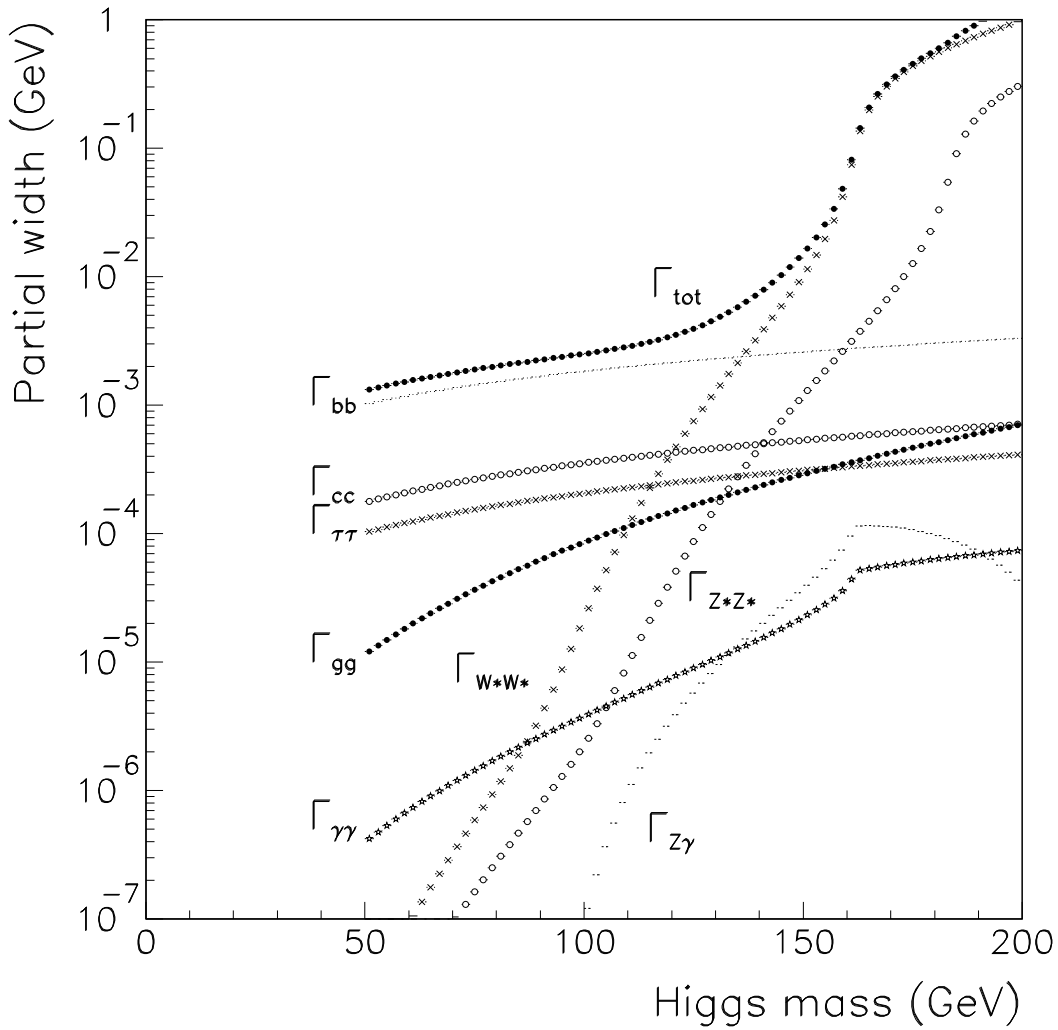


Figure 4: The partial widths of the Higgs boson for $50 \leq m_{H^0} \leq 200$ GeV. Note that the total width is small compared to m_{H^0} up to ~ 200 GeV. The predominant decay widths are $\Gamma_{b\bar{b}}$ and $\Gamma_{W^*W^*}$. $\Gamma_{\gamma\gamma}$ is small but the distinct 2γ signature aids in the reduction of backgrounds.

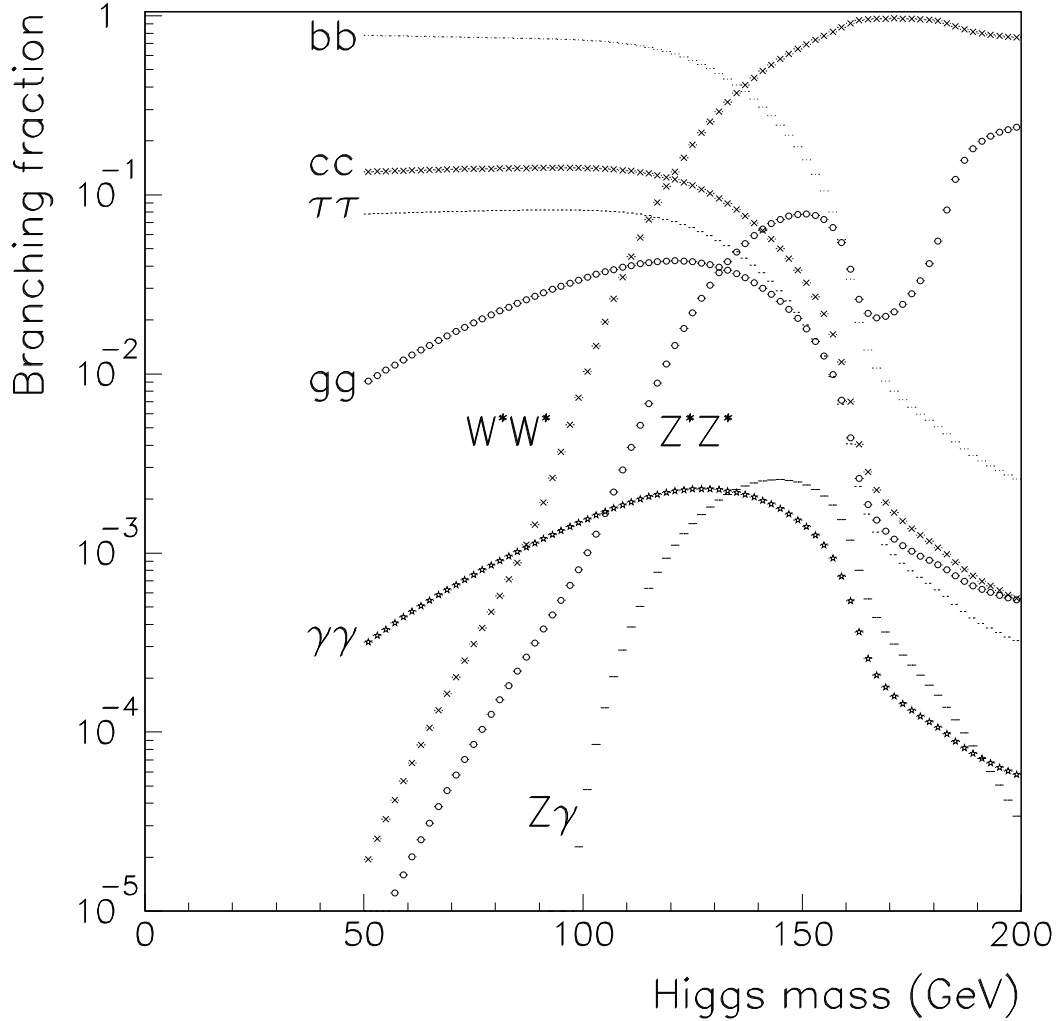


Figure 5: The branching fractions for decay modes of the Higgs boson. The Higgs decays mainly into quark jets ($b\bar{b}$) and modes with missing transverse energy (W^*W^*). The dominance of the W^*W^* mode above $m_{H^0} = 150$ GeV is clear here. If the c-quark mass is treated in the same way as the b-quark $BR_{c\bar{c}}$ will be less than $BR_{\tau\tau}$ in this mass range.

Table 2: Number of $gg \rightarrow H^\circ \rightarrow \gamma\gamma$ events in one LHC year for various Higgs masses.

Higgs mass (GeV)	Number of events
50	1500
75	2250
100	3250
120	3750
150	1800
175	140

where $\tau = m_{H^\circ}^2/s^2$, s is the centre of mass energy squared of the collider and Γ_{gg} is from equation 12, given in appendix A. The higher order corrections in section 3.1 are not used. The term $f(x, Q^2)$, the gluon structure function, is the probability of a gluon carrying a fraction of proton momentum ‘ x ’ at energy scale ‘ Q^2 ’. An external package [24] is accessed to obtain the structure function values. The production cross section as a function of Higgs mass and varying top quark mass (m_t) is shown in figure 6. The cross section curves are high at $m_{H^\circ} < 100$ GeV where the gluon probabilities are high at such low values of ‘ x ’. The cross section increases as m_{H° approaches $2m_t$ because $gg \rightarrow H^\circ$ is mediated by quark loops and the strength is dependent on m_q . The general decrease in cross section after $m_{H^\circ} \sim 2m_t$ is due to decreasing gluon structure function values.

The cross section for $pp(gg) \rightarrow H^\circ \rightarrow \gamma\gamma$ assuming a narrow Higgs resonance is calculated by multiplying equation 1 by $\Gamma_{\gamma\gamma}$ and is shown in figure 7. The number of events due to $pp(gg) \rightarrow H^\circ \rightarrow \gamma\gamma$ expected in one LHC year is calculated and shown in table 2. As can be seen from table 2 and figure 7 a maximum of 3750 $gg \rightarrow H^\circ \rightarrow \gamma\gamma$ events are expected at $m_{H^\circ} = 120$ GeV.

4.3 Simulation of $H^\circ \rightarrow \gamma\gamma$ events

Production of a Higgs boson of m_{H° through gluon-gluon fusion is simulated in the following manner. A proton collider environment is simulated assuming a collision between two protons of equal longitudinal momentum. Since the proton is considered a composite particle at this energy scale the fractions of the total momentum carried by the constituent partons are described by structure functions. A random number (x_1) is generated that reflects the fraction of longitudinal proton momentum carried by gluon (g_1). A second number (x_2) is obtained using the relation

$$M_{H^\circ}^2 = x_1 x_2 s. \quad (2)$$

This relation ensures that the energy in the gluon centre of mass frame is always m_{H° and a Higgs boson is produced.

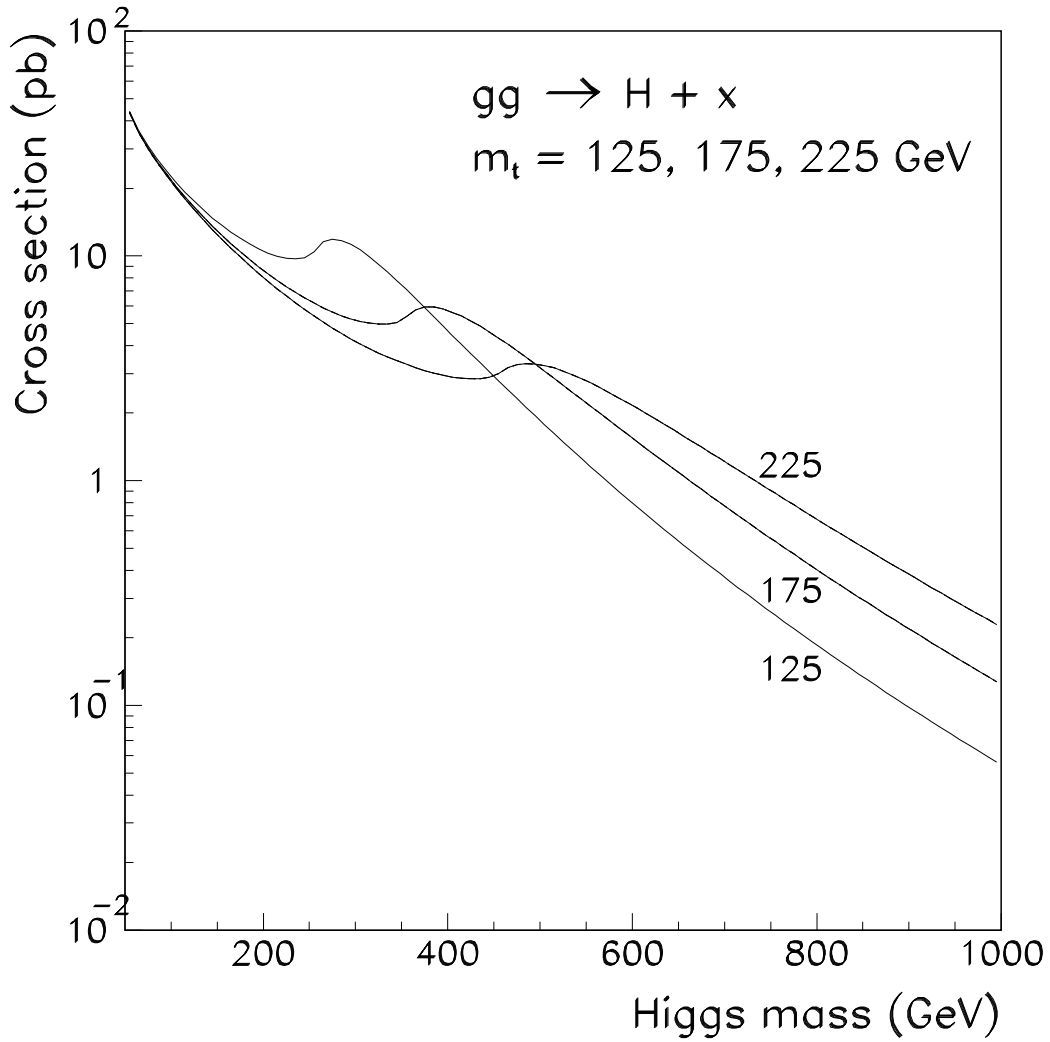


Figure 6: Cross section for $gg \rightarrow H^\circ$ at $\sqrt{s} = 14 \text{ TeV}$ and varying top quark masses. The characteristic bump occurs in each curve at $m_{H^\circ} > 2m_t$. Here the dominant coupling of the Higgs boson to the top quark becomes possible.

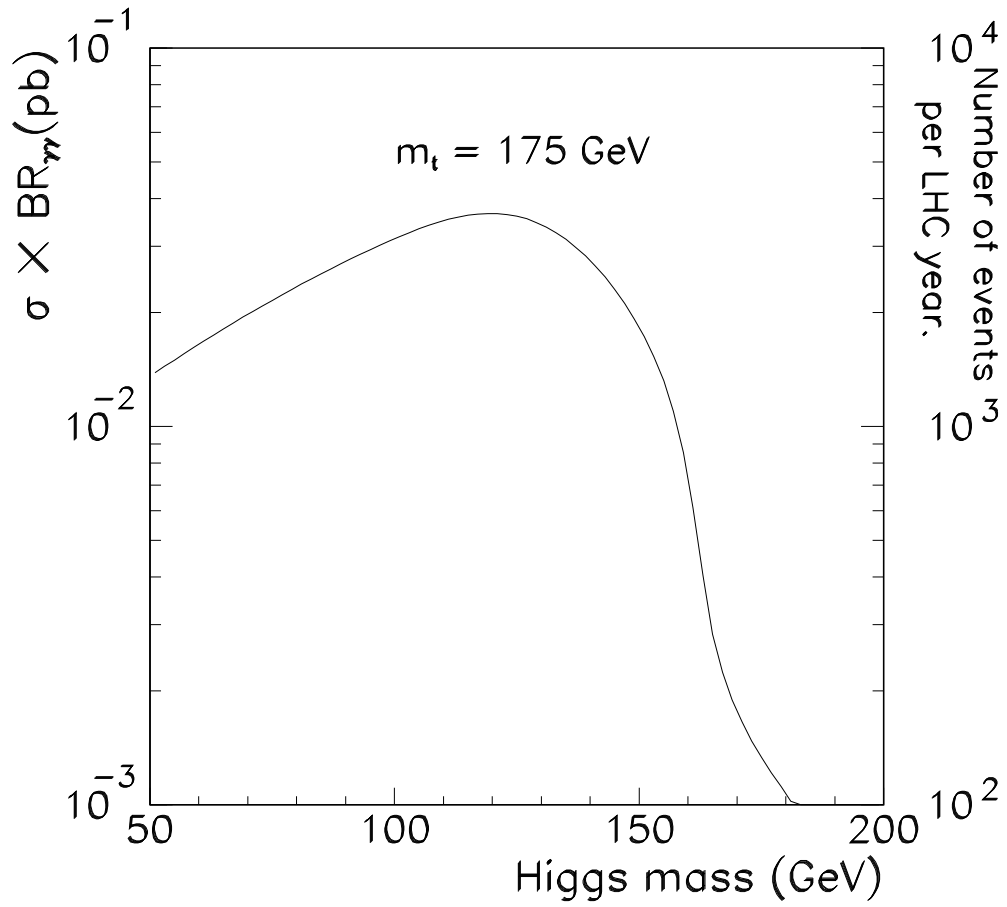


Figure 7: The cross section for $gg \rightarrow H^0 \rightarrow \gamma\gamma$. The left axis gives the cross section in pb, the right axis gives the number of $gg \rightarrow H^0 \rightarrow \gamma\gamma$ events per LHC year (10^7 s).

The range of x_1 is selected to optimize two important considerations:

- The event weights produced by events generated by x_1, x_2 must produce a cross section, averaged over events, compatible with the calculated cross section.
- The problem of machine precision when adding very small weights to very large weights must be solved.

We can use

$$\frac{d\sigma}{dx} = \Gamma_{gg} \frac{\pi^2 \tau}{8 m_{H^0}} \frac{f(x, m_{H^0}^2) f(\frac{\tau}{x}, m_{H^0}^2)}{x} \quad (3)$$

which rises steeply to a maximum at x_{\max} and then monotonically decreases as the *event weight*. Equation 3 is integrated over an x range (x_a, x_b) centered on x_{\max} and bound below by τ until 99% of $d\sigma/dx$ is found. This procedure generally eliminates high x values. Once this condition is met the random variable x_1 is generated uniformly between (x_a, x_b) .

The random number x_1 , generated uniformly on the interval (x_a, x_b) , and associated x_2 have the following properties:

- x_1 is in $(\tau, 1)$ and hence using equation 2 x_2 is also bounded by $(\tau, 1)$. These results assure that Higgs bosons generated using x_1, x_2 are physically allowed.
- The value $d\sigma/dx$ is calculated on an event to event basis. The cross section is obtained by summing over events,

$$\sigma = (x_b - x_a) \sum \left\langle \frac{d\sigma}{dx} \right\rangle$$

- The problem of machine precision is solved by cutting out the high x values that have a low weight, by the procedure mentioned above. These low weights are missed when added to very high weights due to limitations in machine accuracy. If these values are to be included the random numbers cannot be generated with a flat distribution.

At this stage in the simulation the Higgs bosons are stored as 4-vectors $P = \{E_H, \vec{p}_H\}$ where \vec{p}_H is the Higgs boson momentum in the lab frame. Higgs boson momentum in the laboratory frame is calculated by

$$\vec{p}_H = (x_1 - x_2) \vec{p} \quad (4)$$

where \vec{p} is the lab frame momentum of the proton associated with x_1 . This momentum is entirely along the beam line since only the longitudinal momentum of the protons is considered and higher order real corrections are not applied [22].

Every Higgs boson is decayed into 2 photons (γ_1, γ_2) that will be back to back and isotropic in the Higgs boson rest frame. This decay is simulated by generating a pair of back to back unit vectors $\hat{v}_i = x_i \hat{x} + y_i \hat{y} + z_i \hat{z}$ ($i = 1, 2$) that represent γ_1, γ_2 . These vectors are uniformly distributed over a sphere. In the Higgs boson rest frame the 4-vector of γ_i is

$$P_{\gamma_i}^{\text{CM}} = \left\{ \frac{m_{H^0}}{2}, \frac{m_{H^0}}{2} (\hat{v}_i) \right\}.$$

These photon 4-vectors are Lorentz boosted by \vec{p}_H from equation 4 producing photon 4-vectors in the laboratory frame P_{γ_i} . Each Higgs boson produces two boosted photon 4-vectors

P_{γ_i} defined in a right-handed coordinate system with \hat{z} aligned with the incoming proton associated with x_1 . The *reconstructed Higgs mass* is easily obtained from the invariant mass of the photon 4-vectors P_{γ_i} .

4.4 Detector response to $H^0 \rightarrow \gamma \gamma$

Before the reconstructed Higgs masses can be studied a brief description of the calorimeter is needed. The calorimeter is a cylinder that covers 72% of the solid angle. Thus photons that miss this region are not studied, this is the *acceptance cut*. The identification efficiency of photons that are incident on the calorimeter is assumed to be 100%. All the energy of the γ 's is assumed to be deposited in this calorimeter and is then smeared as described below. Since the angle of photons is known from P_{γ_i} the calorimeter measures this angle identically.

Detector response to photons is simulated next. A calorimeter is capable of giving the energy (E_i) and direction (θ_i, ϕ_i) of γ_i . The accuracy in measuring energy and direction is given by the energy (in GeV) and angular resolutions

$$\begin{aligned} \frac{\sigma_E}{E} &= \frac{a}{\sqrt{E}} \oplus b \oplus \frac{c}{E} \text{ (\%)} \\ \sigma_\theta &= \frac{d}{\sqrt{E}} \oplus e \oplus \frac{f}{E} \text{ (rad)} \\ \sigma_\phi &= \frac{g}{\sqrt{E}} \oplus h \oplus \frac{j}{E} \text{ (rad)} \end{aligned} \tag{5}$$

respectively (\oplus denotes addition in quadrature). Constants 'a' through 'j' are parameters of the calorimeter performance and do not vary between events.

The components of P_{γ_i} are converted from cartesian to spherical coordinates yielding E_i , θ_i and ϕ_i . A routine that independently smears E_i , θ_i and ϕ_i simulates the calorimeter response to photons. Each of E_i , θ_i and ϕ_i is smeared using

$$\begin{aligned} E_i^{\text{smeared}} &= E_i + \delta_{E_i} \text{ (GeV)} \\ \theta_i^{\text{smeared}} &= \theta_i + \delta_{\theta_i} \text{ (rad)} \\ \phi_i^{\text{smeared}} &= \phi_i + \delta_{\phi_i} \text{ (rad)} \end{aligned} \tag{6}$$

where δ_{E_i} , δ_{θ_i} and δ_{ϕ_i} are calculated for each γ_i . The δ 's are generated by multiplying three random numbers from a normal distribution with σ_{E_i} , σ_{θ_i} and σ_{ϕ_i} respectively. The constants used to simulate the calorimeter performance [25] in equations 5 are shown in table 3. Pile-up of events, caused by the high luminosity of the collider (section 2.1), and its effect on energy resolution is not simulated here.

Table 3: Energy and angular resolutions used in light Higgs study. Experimental values from [25] are used (E is in GeV).

Quantity	Expression
$\frac{\sigma_E}{E}(\%)$	$\frac{10\%}{\sqrt{E}} \oplus 0.6 \oplus \frac{0.319}{E}$
$\sigma_\theta(\text{mrad})$	$\frac{25}{\sqrt{E}} \oplus 3 \oplus \frac{76}{E}$
$\sigma_\phi(\text{mrad})$	$\frac{36}{\sqrt{E}} \oplus 2 \oplus \frac{131}{E}$

Table 4: Acceptance, mass resolution and $\sigma \times \text{BR}$ for various Higgs masses.

Higgs mass (GeV)	90	110	120	130	150	200
Acceptance (%)	28.6	40.9	44.2	46.9	50.5	55.9
$\sigma \times \text{BR}$ (fb)	24.8	30.5	31.4	28.9	15.0	0.4
Mass resolution (%)	1.08	0.97	0.98	0.94	0.87	0.84

4.5 Kinematic cuts

Following references [20, 26] we use the following cuts:

- For each photon $P_T > 40$ GeV. This cut sets the trigger threshold of the calorimeter system;
- Both photons are required to be within the ATLAS barrel electromagnetic calorimeter. This is achieved by requiring $-2 < \eta < 2$ where

$$\eta = -\ln\left(\tan\frac{\theta}{2}\right),$$

where θ is the polar angle.

There is no asymmetry in P_T for the photons so a cut on asymmetric P_T in [25] is not used. The acceptances obtained with these cuts are shown in table 4.

4.6 Results

The effects on the reconstructed Higgs mass due to smearing E , θ and ϕ in the light Higgs range $90 \leq m_{H^0} \leq 200$ GeV are shown in figure 8. The resolutions used are shown in table 3 and are indicative of the performance of the calorimeter system in ATLAS. The acceptance cut and the cuts described in section 3.2 are applied to the photons in this study.

In figure 8 the relative effects of each experimental resolution can be seen. The energy resolution (figure 8(b)) is the dominant factor in reconstructing the Higgs mass from two

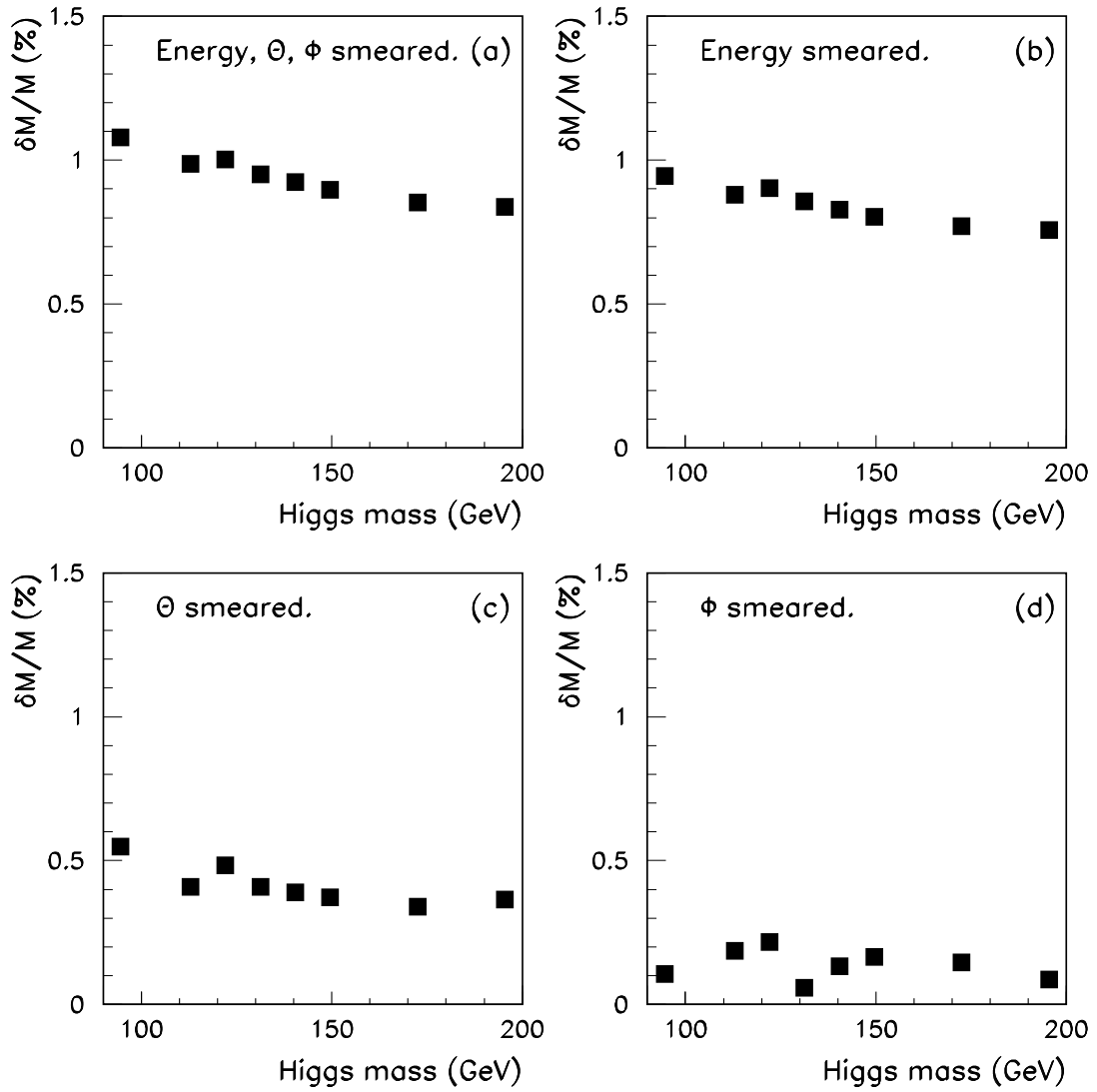


Figure 8: The Higgs mass resolution as a percentage versus Higgs mass. (a) Energy, θ and ϕ smeared. (b) Energy smeared only. (c) θ smeared only. (d) ϕ smeared only. The resolutions used in the smearing are shown in table 3.

photons. Next in importance is θ resolution (σ_θ), see figure 8(c). The θ smearing predicts that $\delta m_{H^0}/m_{H^0}$ due to σ_θ is about half that due to energy resolution. The effect of σ_ϕ (figure 8(d)) is the least here. The value of σ_ϕ is comparable to σ_θ (see table 3) but the fact that the photons are back to back in the $r - \phi$ plane lessens the effect. Figure 8(a) shows the effect of smearing all quantities and it can be seen that the Higgs mass resolution is in the 1% range for this mass range. It has been shown [13, 26] that such a mass resolution is needed in order to see the Higgs signal over the large background.

Next the effect on $\delta m_{H^0}/m_{H^0}$ by varying the energy and θ resolutions is studied. In figure 7 and table 2 it is seen that the most Higgs events are generated with $m_{H^0} = 120$ GeV. The effect of ϕ resolution is not studied since the effect is seen to be minimal as shown above. The results of this study are shown in figure 9.

Looking at figure 9(a) the effect on $\delta m_{H^0}/m_{H^0}$ due to increasing σ_θ is noticeable. The same effect can be seen in figure 9(b) where the energy resolution is increased. In figure 9(a) a nominal Higgs mass resolution of 1.2%, with the given experimental resolutions, is achieved with an angular resolution sampling term of $100 \text{ mrad} \cdot \text{GeV}^{\frac{1}{2}}$. A $100 \text{ mrad} \cdot \text{GeV}^{\frac{1}{2}}$ angular sampling term can be considered the benchmark for angular performance of the calorimeter system. To achieve the same nominal Higgs mass resolution with the given resolutions an energy resolution sampling term of $13\% \cdot \text{GeV}^{\frac{1}{2}}$ is needed as shown in figure 9(b). This study was repeated with the resolution values from [26] and the results agree.

The longitudinal momentum (P_L) of the Higgs boson is another interesting quantity. Knowledge of P_L for different Higgs masses gives the angular distribution of the photons. Thus the number of photons kept by a particular acceptance cut is known. The longitudinal momentum of different Higgs masses is compared by observing the rms (width) of the P_L distribution, shown in figure 10.

Figure 10 clearly shows that the P_L width increases with mass. This can be explained from the behaviour of the gluon structure functions. As the Higgs mass increases larger values of 'x' can produce a Higgs boson. There is still a high probability of a low x_1 gluon and a high x_2 forming a Higgs boson. The large difference in x_1 and x_2 produces this longitudinal momentum. Thus the decay particles of a heavy Higgs boson have a high probability of travelling close to the beam line. For the mass range where $H^0 \rightarrow \gamma \gamma$ is an attractive decay ($50 \leq m_{H^0} \leq 200$ GeV) significant P_L is seen. By maximizing the fraction of solid angle equipped able to detect photons accurately the probability of detecting this decay is increased.

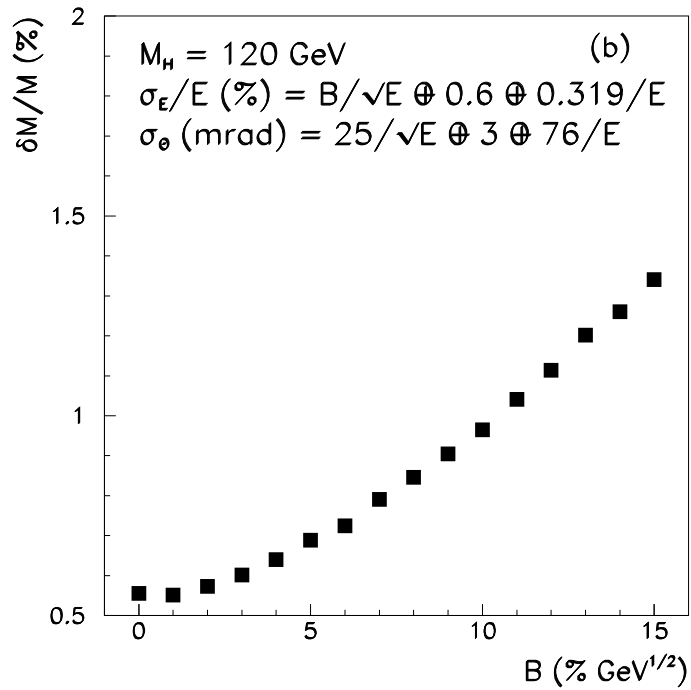
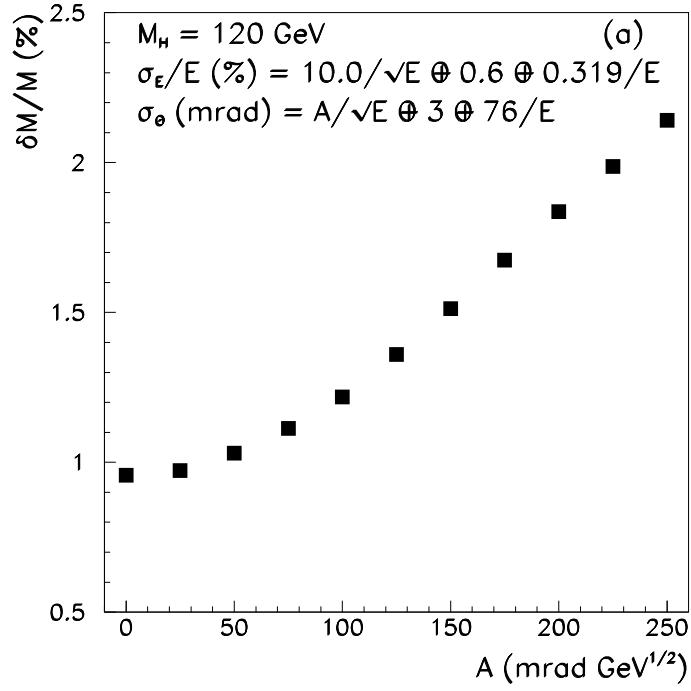


Figure 9: Higgs mass resolution as a percentage versus; (a) angular resolution sampling term, (b) energy resolution sampling term. In both cases a Higgs mass of 120 GeV is studied.

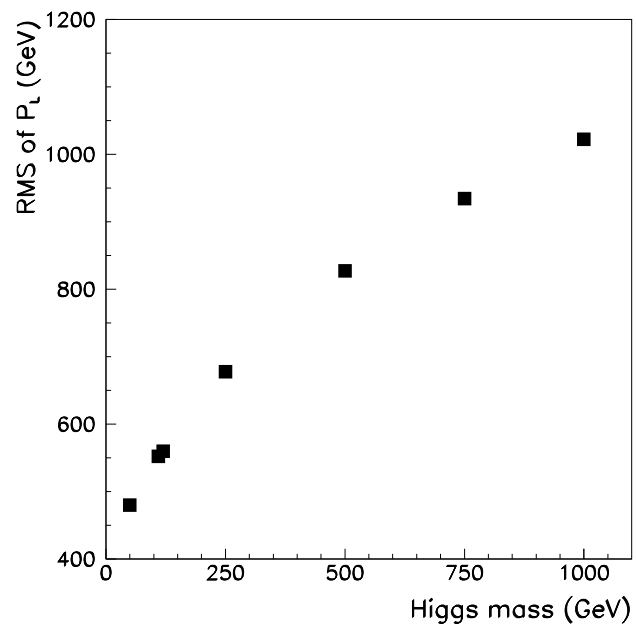


Figure 10: rms of the Higgs boson longitudinal momentum (P_L) versus Higgs mass. Note the rms increases with the Higgs mass.

5 Conclusions

In this study the production and decay of Higgs particles at a $p\bar{p}$ collider was studied. In particular the production process $gg \rightarrow H^\circ$ and the decay process $H^\circ \rightarrow \gamma\gamma$ was studied. The partial widths and branching fractions of some important decay processes were calculated. The Higgs total width was found to be narrow in the region of interest ($90 \leq m_{H^\circ} \leq 200$ GeV) for the $H^\circ \rightarrow \gamma\gamma$ decay. The lowest order cross section for $gg \rightarrow H^\circ$ was calculated and using the partial width for $H^\circ \rightarrow \gamma\gamma$, the cross section for $gg \rightarrow H^\circ \rightarrow \gamma\gamma$ was calculated. Using the LHC parameters the number of such events was calculated and found to be in the order of 10^3 per LHC year.

The longitudinal momentum spectrum of the Higgs boson was studied and the width of the distribution was found to increase with Higgs mass. This is understood when the behaviour of the gluon structure functions are considered. The acceptances of photons for various Higgs masses were found to agree with published results [13, 20].

A simulation of Higgs particles decaying exclusively to two photons was performed and the effects of various experimental calorimeter resolutions on the reconstructed Higgs mass were studied. The ATLAS calorimeter system [14], that has resolutions shown in table 3, can reconstruct m_{H° to $\sim 1\%$ accuracy (needed to see the Higgs particle over the large background) in the light Higgs mass range. The importance of both good energy and θ resolution is demonstrated and a more sophisticated simulation might point to an important σ_ϕ relationship.

The effects of varying energy and θ resolutions was studied. To maintain a nominal Higgs mass resolution of 1.2% the angular resolution sampling term has to be $100 \text{ mrad} \cdot \text{GeV}^{\frac{1}{2}}$, given the energy resolution from [25]. Conversely an energy resolution sampling term of $13\% \cdot \text{GeV}^{\frac{1}{2}}$ is needed to give the same nominal mass resolution, given the experimental θ resolution from [25]. This study was repeated using the resolution values in [26] and the results agreed. The most recent test beam performance figures of the ATLAS barrel electromagnetic calorimeter system [25] surpass the basic requirements [26] to detect the light Higgs boson.

A Partial width formulae

The following formulae are used to calculate the partial widths of the Higgs boson. The $H^\circ \rightarrow \gamma \gamma$ partial width is given by [11]

$$\Gamma_{\gamma\gamma} = \frac{\alpha^2 g^2}{1024\pi^3} \frac{m_{H^\circ}^3}{m_W^2} \left| \sum N_{ci} e_i^2 F_i \right|^2 \quad (7)$$

where i is the spin $\frac{1}{2}$ and spin 1 particles, e_i is electric charge in units of e and N_{ci} is a colour factor (3 for quarks and 1 for leptons). The function F_i is defined as

$$F_{\frac{1}{2}} = -2\tau(1 + (1 - \tau)f(\tau))$$

$$F_1 = 2 + 3\tau + 3\tau(2 - \tau)f(\tau) \quad (8)$$

$$(9)$$

where

$$\tau = \frac{4m_i^2}{m_{H^\circ}^2}$$

$$f(\tau) = \begin{cases} [\sin^{-1}(\sqrt{1/\tau})]^2 & \text{if } \tau \geq 1 \\ -\frac{1}{4}[\ln(\eta^+/\eta^-) - i\pi]^2 & \text{if } \tau < 1 \end{cases} \quad (10)$$

and

$$\eta^\pm \equiv (1 \pm \sqrt{1 - \tau})$$

The partial width of $H^\circ \rightarrow f\bar{f}$ is calculated using [11]

$$\Gamma_{f\bar{f}} = \frac{N_{ci} g^2 m_f^2}{32\pi m_W^2} \left(1 - \frac{4m_f^2}{m_{H^\circ}^2}\right)^{3/2} m_{H^\circ} \quad (11)$$

where m_f is the mass of the fermion.

The width to gluons is given by [11]

$$\Gamma_{gg} = \frac{\alpha_s^2 g^2 m_{H^\circ}^3}{128\pi^3 m_W^2} \left| \sum \tau_i [1 + (1 - \tau_i)f(\tau_i)] \right|^2 \quad (12)$$

where i is an index for each quark, τ_i and $f(\tau_i)$ are defined as in equations 10. Since only the gluons and quarks carry colour charge there can only be quarks in the loop.

The $Z\gamma$ partial width [11] is shown next. This decay could be useful to detect the Higgs boson in the light mass range if the backgrounds can be identified and cut.

$$\Gamma_{Z\gamma} = \frac{1}{32\pi} |\mathcal{A}|^2 m_{H^\circ}^3 \left(1 - \frac{m_Z^2}{m_{H^\circ}^2}\right)^3 \quad (13)$$

where

$$\mathcal{A} = \frac{\alpha g}{4\pi m_W} \left(-\cot \theta_W \left\{ 4(3 - \tan^2 \theta_W) I_2(\tau_W, \lambda_W) + \left[\left(1 + \frac{2}{\tau_W}\right) \tan^2 \theta_W - \left(5 + \frac{2}{\tau_W}\right) \right] I_1(\tau_W, \lambda_W) \right\} \right)$$

with $\tau_W \equiv \frac{4m_W^2}{m_{H^\circ}^2}$ and $\lambda_W \equiv \frac{4m_W^2}{m_Z^2}$.

The integrals I_1, I_2 have been evaluated explicitly

$$I_1(a, b) = \frac{ab}{2(a-b)} + \frac{(ab)^2}{2(a-b)^2}[f(a) - f(b)] + \frac{a^2b}{(a-b)^2}[g(a) - g(b)]$$

$$I_2(a, b) = \frac{-ab}{2(a-b)}[f(a) - f(b)]$$

where

$$g(\tau) = \begin{cases} [\sqrt{1-\tau} \sin^{-1}(\sqrt{1/\tau})]^2 & \text{if } \tau \geq 1 \\ \frac{1}{2}\sqrt{1-\tau} [\ln(\eta^+/\eta^-) - i\pi]^2 & \text{if } \tau < 1 \end{cases}$$

and $f(\tau)$ and η^\pm are defined as in equations 10.

For $H^\circ \rightarrow W^*W^* \rightarrow \bar{\ell}_1\bar{\ell}'_2\bar{\ell}_3\bar{\ell}'_4$ the formula is [27]

$$\Gamma_{W^*W^*} = \frac{g^6 m_W^2}{2^{14} 3^2 \pi^5 m_{H^\circ}} \int_0^1 \frac{dx_1}{[(x_1 - \epsilon^2)^2 + (\epsilon\delta)^2]} \int_0^{(1-\sqrt{x_1})} dx_2 \frac{\lambda^{1/2}(1; x_1, x_2)[\lambda(1; x_1, x_2) + 12x_1x_2]}{[(x_2 - \epsilon^2)^2 + (\epsilon\delta)^2]} \quad (14)$$

where

$$x_1 = \left(\frac{m_1}{m_{H^\circ}}\right)^2 \quad x_2 = \left(\frac{m_2}{m_{H^\circ}}\right)^2 \quad \epsilon \equiv \frac{m_W}{m_{H^\circ}} \quad \delta \equiv \frac{\Gamma_W}{m_W}$$

and λ , a quantity found in calculating phase space integrals [27], is given by

$$\lambda(1; x_1, x_2) = \left[1 - \frac{(m_1 + m_2)^2}{s}\right] \left[1 - \frac{(m_1 - m_2)^2}{s}\right].$$

For $H^\circ \rightarrow Z^*Z^* \rightarrow \bar{\ell}_a\bar{\ell}'_a\bar{\ell}_b\bar{\ell}'_b$ the width is related to $\Gamma_{W^*W^*}$ by

$$\Gamma_{Z^*Z^*} = C_a C_b (g_V^{a^2} + g_A^{a^2})(g_V^{b^2} + g_A^{b^2}) \Gamma_{W^*W^*}$$

where $\Gamma_{W^*W^*}$ is defined in equation 14. C_a, C_b are colour factors defined in the same way as N_{ci} above and $g_V^a, g_A^a, g_V^b, g_A^b$ are the vector and axial coupling constants of fermions a and b respectively.

References

- [1] S. L. Glashow, Partial-Symmetries of Weak Interactions. *Nucl. Phys.*, **22** (1961), p.579; A. Salam in Elementary Particle Theory. ed. N. Svartholm. (Almqvist and Wiksell, Stockholm, 1968); S. Weinberg, A Model of Leptons *Phys. Rev. Lett.*, **19** (1967), p.1264.
- [2] G. Arnison *et al.*, Experimental Observation of Isolated Large Transverse Energy Electrons with Associated Missing Energy at $\sqrt{s} = 540$ GeV. *Phys. Lett.*, 122B (1983), p.103.
- [3] G. Arnison *et al.*, Experimental Observation of Lepton Pairs of Invariant Mass Around $95\text{GeV}/c^2$ at the CERN SPS Collider. *Phys. Lett.*, 126B (1983), p.398.
- [4] Particle Data Group, Review of Particle Properties. *Physical Review D: Particles and Fields*, **45D** (1992).
- [5] The CDF collaboration, Evidence for Top Quark production in $p\bar{p}$ collisions at $\sqrt{s} = 1.8$ TeV. FERMILAB-PUB-94/097-E (1994).
- [6] M. Kobayashi and T. Maskawa, CP-Violation in the Renormalizable Theory of Weak Interaction. *Prog. Theor. Phys.*, **49**, (1973), p.652. N. Cabibbo, Unitary Symmetry and Leptonic Decays. *Phys. Rev. Lett.*, **10**, (1963), p.531.
- [7] See for example the following review:
J. R. Carter, *Precision tests of the Standard Model at LEP*, Proceedings of The Joint International Lepton-Photon Symposium and Europhysics Conference on High Energy Physics, Geneva, Switzerland, 25 July - 1 August 1991, World Scientific.
- [8] The LEP Electroweak Working Group,
Updated Parameters of the Z^0 Resonance from Combined Preliminary Data of the LEP Experiments. CERN/PPE/93-157, 26 August, 1993
- [9] P. W. Higgs, Broken Symmetries, Massless Particles and Gauge Fields. *Phys. Lett.*, **12** (1964), p.132.
Broken Symmetries and the Masses of the Gauge Bosons. *Phys. Rev. Lett.*, **13** (1964), p.508.
Spontaneous Symmetry Breakdown without Massless Bosons. *Phys. Rev.*, **145** (1966), p.1156.
- [10] G. 't Hooft, Renormalization of massless Yang-Mills fields. *Nucl. Phys.*, **B33** (1971), p.173.
Renormalizable Lagrangians for massive Yang-Mills fields. *Nucl. Phys.* (1971), **B35**, p.167.
- [11] For reviews, see:
M. Sher, Electroweak Higgs Potentials and Vacuum Stability. *Phys. Rep.*, **179** (1989), p.273. and
J. Gunion *et al.*, *The Higgs Hunter's Guide.*, (Addison-Wesley, Redwood City, 1990).
- [12] A. Carter, talk given at the IoP Conference on Nuclear and Particle Physics, Glasgow, 1993.
- [13] The LHC Study Group, *Design Study of the Large Hadron Collider (LHC)*, CERN/91-03, 2 May 1991.
- [14] The ATLAS Collaboration, *Letter of Intent*, CERN/LHCC/92-4, LHCC/I 2, 1 October 1992.

- [15] For a general overview of physics, detectors and detector subsystems at future hadron colliders see,
P. Jenni and J. White, Physics and Experimental Challenge of Future Hadron Colliders. *Proceedings of the 1993 Lake Louise Winter Institute.*, held in Lake Louise, Alberta, 21st to 27th of February, 1993.
- [16] M. Della Negra *et al*, The Standard Model Higgs at LHC: Branching Ratios and Cross-Sections. Proceedings of the Large Hadron Collider workshop, **Vol II CERN 90-10** (1990), p.509.
- [17] J. Ellis, G. L. Fogli and E. Lisi, The Top Quark and Higgs Boson Masses in the Standard Model and MSSM. **CERN-TH 7261/94**, May 1994.
- [18] D. Graudenz *et al*, QCD Corrections to Higgs-boson Production at Proton-Proton Colliders. *Phys. Rev. Lett.*, **70** (1993), p.1372.
- [19] For a review of structure functions see D. Perkins, *Introduction to high energy physics*, (3rd ed.) (Addison-Wesley Publishing Company. Menlo Park, 1987), p.266-283.
- [20] C. Seez and T. Virdee, The Standard Model Higgs at LHC: Branching Ratios and Cross-Sections. Proceedings of the Large Hadron Collider workshop, **Vol II CERN 90-10** (1990), p.474.
- [21] Z. Kunszt and W. J. Stirling, The Standard Model Higgs at LHC: Branching Ratios and Cross-Sections. Proceedings of the Large Hadron Collider workshop, **Vol II CERN 90-10** (1990), p.427.
- [22] M. Spira *et al*, SUSY Higgs production at proton colliders. *Phys. Lett.*, **B318** (1993), p.347.
- [23] H. Baer *et al*, Observability of $\gamma\gamma$ decays of Higgs bosons from supersymmetry at hadron supercolliders. *Phys. Rev.*, **D46** (1992), p.1067.
- [24] H. Plochow-Besch, PDFLIB: A library of all available Parton Density Functions of the Nucleon, the Pion and the photon and the corresponding α_s calculations. CERN-PPE/92-123.
- [25] B. Aubert *et al.*, Performance of a Liquid Argon Preshower Detector Integrated with an Accordion Calorimeter. *Nucl. Inst. and Meth.*, **A330** (1993), p.405-415.
- [26] L. Fayard, and G. Unal, Search for Higgs Decay into Photons with EAGLE. EAGLE note, PHYS-NO-001.
- [27] Michel Lefebvre, private communication.